A finite element study of the piezo-poroelastic sound package concept

Cédric Batifol, Tomasz Zielinski, Mohamed Ichchou, Marie-Annick Galland

A finite-element study of a piezoelectric/poroelastic sound package concept

C Batifol[1,2], T G Zielinski[3], M N Ichchou[1] and M-A Galland[2]

[1] Laboratoire de Tribologie et Dynamique des Syst`emes, Ecole Centrale de Lyon-36, Avenue Guy de Collongue, 69130 Ecully, France

[2] Laboratoire de M´ecanique des Fluides et d'Acoustique, Ecole Centrale de Lyon-36, Avenue Guy de Collongue, 69130 Ecully, France

[3] Institute of Fundamental Technological Research, Polish Academy of Sciences, Swietokrzyska 21, 00-049 Warszawa, Poland

Abstract

This paper presents a complete finite-element description of a hybrid passive/active sound package concept for acoustic insulation. The sandwich created includes a poroelastic core and piezoelectric patches to ensure high panel performance over the medium/high and low frequencies, respectively. All layers are modelled thanks to a *Comsol* environment[4]. The piezoelectric/elastic and poroelastic/elastic coupling are fully considered. The study highlights the reliability of the model by comparing results with those obtained from the *Ansys* finite-element software and with analytical developments. The chosen shape functions and mesh convergence rate for each layer are discussed in terms of dynamic behaviour. Several layer configurations are then tested, with the aim of designing the panel and its hybrid functionality in an optimal manner. The differences in frequency responses are discussed from a physical perspective. Lastly, an initial experimental test shows the concept to be promising.

1. Introduction

Multilayered panels are widely used as solutions for limiting the transmission of acoustic waves. These so-called 'sandwiches' are made up of two elastic materials and a core. The simplest core could be an airgap, but highly dissipative media such as poroelastic materials would make the best candidates. Such passive panels are efficient enough at medium and high frequencies but exhibit a lack of performance at low frequency, where resonance inherent to the layer distribution occurs. Active control appears to be the right approach for remedying this problem. Piezoelectric patches are added to the panel and behave as a secondary vibrational source, interfering with the low frequency disturbance propagating in the panel.

[4] *Comsol* is the new name of the finite element software previously called *Femlab*.

The first major investigations on this hybrid concept were conducted by Guigou [1] and Fuller [2]. The purpose therein was to reduce sound transmitted into an aircraft. Two configurations were proposed: a smart skin composed of piezoelectric actuators bonded onto a polyurethane foam, and a secondary 'speaker diaphragm' driven by two bimorph active beams. Double panel systems were proposed a few years later. Carneal [3] developed a robust analytical model of a simply supported plate–air–plate system. Prediction of the transmission losses (TL_{dB}) was compared with measurements performed on a specific test bench. An initial parametric work was aimed at finding the best placement for piezoelectric patches.

The present study has taken advantages of new solutions developed at Ecole Centrale de Lyon for the design of a hybrid broadband absorbing liner, which associates the

passive properties of porous materials with active control [4]. The concept is to be adapted herein to sound insulation. The widespread design of such active/passive mufflers is still an open topic, which may now be addressed thanks to the development of new predictive tools. Recent advances allow modelling the complete harmonic poroelastic problem using the finite-element method [5]. The well-adapted formulation has been implemented within the *Comsol* environment. Coupling this formulation with elastic, acoustic and piezoelectric application modes provided by *Comsol* offers the possibility to directly solve the multiphysics harmonic problem of multilayered mufflers.

In this paper, the results presented will focus first on the high reliability of each layer model. The *Comsol* formulation for poroelastic material is described completely; this implies equations for both the Neumann and Dirichlet boundary conditions. The model is validated by describing results for the analytically solved case of a one-dimensional (1D) porous layer bonded onto a rigid wall. The pertinent shape functions and converged mesh are discussed in terms of dynamic layer behaviour. A rather similar discussion is then conducted regarding the coupled piezoelectric/elastic problem. The forced response of these two-layer arrangements is calculated thanks to a *Comsol* and *Ansys* software application for two different geometries. Limitations arising from calculation costs will also be highlighted.

The second part of this paper studies the dynamic response of the whole sandwich assembly. The properties of different layers are tested; these involve changes in elasticity moduli, damping factors and piezoelectric matrices. The complete coupling with fluid media (air) allows calculating efficiency indicators, such as transmission loss (TL_{dB}). Differences are then investigated in terms of resonant behaviour of the panel. Conclusions lead first to discussions on ideal active patches (properties and position) and the passive poroelastic core. Lastly, initial experimental measurements of the transmission losses are performed on a specific set-up, with results being compared to those obtained numerically from the new finite-element code.

2. Poroelasticity modelling

2.1. Motion equations

Comsol does not currently provide a specific application mode for poroelasticity. In problems where the hypothesis of a rigid skeleton for porous media is valid, the pre-established acoustic application mode can obviously be used to implement the *fluid-equivalent* model of the porous layer. The study developed here does not allow for this assumption to be adopted since the active control procedure must be efficient over low frequencies, where strong coupling between the fluid and solid phases of the poroelastic material occurs. The biphasic theory introduced by Biot in [6] then becomes necessary. The classical formulation involves two unknown fields, $\underline{u}^{\mathrm{s}}$ and $\underline{U}^{\mathrm{f}}$, which stand for the frame and the fluid displacements, respectively[5]. For a three-dimensional (3D) discretized problem, six degrees of freedom per node are present. Considering the fact that the behaviour of such a material is frequency dependent, a sizeable calculation time is needed, which prevents a parametric study from being conducted. In 1998, Atalla *et al* [7] introduced the new ($\underline{u}^{\mathrm{s}}$, p) formulation, valid only for harmonic motion. No new assumptions were adopted for comparison with Biot's formulation, and only four degrees of freedom remain since the fluid phase is described by means of the pore pressure.

Implementation is performed by directly programming the ($\underline{u}^{\mathrm{s}}$,$p$) formulation under *Comsol*'s general partial differential equation (PDE) mode. The partial differential equations have to be rewritten in order to fit the software standard detailed in equation (1).

$$\begin{aligned} \underline{\underline{\Gamma}} \cdot \underline{\nabla} &= \underline{F} \qquad \text{in } \Omega, \\ -\underline{n} \cdot \underline{\underline{\Gamma}} &= \underline{G} + \left(\frac{\partial \underline{R}}{\partial \underline{U}} \right)^T l \qquad \text{on } \partial\Omega_{\mathrm{N}}, \\ 0 &= \underline{R} \qquad \text{on } \partial\Omega_{\mathrm{D}}, \end{aligned} \tag{1}$$

where Ω, $\partial\Omega_{\mathrm{D}}$ and $\partial\Omega_{\mathrm{N}}$ are the calculation domain, Dirichlet boundary and Neumann boundary, respectively. $\underline{U}$ is the vector of unknowns and $\underline{\underline{\Gamma}}$ the equation matrix governing the problem. $\underline{n}$ is the outward normal unit vector, $\underline{R}$ the 'Dirichlet' vector, and $\underline{G}$ the 'Neumann' vector. l denotes the Lagrange multiplier, and lastly $\underline{\nabla}$ is the nabla operator. For the three-dimensional harmonic ($\underline{u}^{\mathrm{s}}$, p) formulation, $\underline{U}$ and $\underline{F}$ are column vectors with four rows, and $\underline{\underline{\Gamma}}$ is a matrix with four rows and three columns. Equations (2) and (3) describe the complete matrices introduced to solve the harmonic problem at an angular frequency of ω. The orthonormal basis is ($\underline{x}_1$, $\underline{x}_2$, $\underline{x}_3$) and the notation $v_{i,j}$ stands for the differentiation operation of the x_i component of vector $\underline{v}$ over x_j. Indices i and j obviously vary from 1 to 3. The summation convention is used, by implying $v_{k,k}$ as the divergence of vector $\underline{v}$.

$$\begin{bmatrix} \Gamma_{ij} \\ \Gamma_{4j} \end{bmatrix} = \begin{bmatrix} \mu_{\mathrm{s}} \left(u^{\mathrm{s}}_{i,j} + u^{\mathrm{s}}_{j,i} \right) + \hat{\lambda}^{\mathrm{s}} u^{\mathrm{s}}_{k,k} \delta_{ij} \\ p_{,j} \end{bmatrix}, \tag{2}$$

$$\begin{bmatrix} F_i \\ F_4 \end{bmatrix} = \begin{bmatrix} -\omega^2 \tilde{\rho} u^{\mathrm{s}}_i - \tilde{\gamma} p_{,i} \\ -\omega^2 \frac{\tilde{\rho}^{22}}{\tilde{\lambda}^{\mathrm{f}}} p + \omega^2 \frac{\tilde{\rho}^{22} \tilde{\gamma}}{\phi^2} u^{\mathrm{s}}_{k,k} \end{bmatrix}, \tag{3}$$

where

$$\hat{\lambda}^{\mathrm{s}} = \tilde{\lambda}^{\mathrm{s}} - \frac{\left(\tilde{\lambda}^{\mathrm{sf}} \right)^2}{\tilde{\lambda}^{\mathrm{f}}}, \tag{4}$$

$$\tilde{\rho} = \tilde{\rho}^{11} - \frac{\left(\tilde{\rho}^{12} \right)^2}{\tilde{\rho}^{22}}, \tag{5}$$

$$\tilde{\gamma} = \phi \left(\frac{\tilde{\rho}^{12}}{\tilde{\rho}^{22}} - \frac{\tilde{\lambda}^{\mathrm{sf}}}{\tilde{\lambda}^{\mathrm{f}}} \right). \tag{6}$$

The above equations entail numerous complex, frequency-dependent, poroelastic parameters. ϕ is the porosity defined as the ratio between fluid phase volume and total volume of the sample. $\hat{\lambda}^{\mathrm{s}}$, μ^{s} and $\tilde{\lambda}^{\mathrm{f}}$ are the two Lamé-like coefficients of the solid phase and the one fluid phase coefficient, respectively. $\tilde{\rho}^{11}$ and $\tilde{\rho}^{22}$ are the relative densities. Coupling between the solid and fluid phases is represented by the two parameters $\tilde{\rho}^{12}$ and $\tilde{\lambda}^{\mathrm{sf}}$. These two coefficients highlight the complex coupling occurring in poroelastic materials. Apart from the classical interaction due to constitutive relations (term $\tilde{\lambda}^{\mathrm{sf}}$), a strong inertial coupling can be represented by $\tilde{\rho}^{12}$. This coupling prevents us from just mixing pre-established acoustic and solid elastic *Comsol* application modes. This is the reason for using the general *PDE* application mode.

[5] In this document '$\underline{\ }$' stands for a vector and '$\underline{\underline{\ }}$' for a matrix.

2.2. Boundary and coupling conditions

To derive a well-expressed formulation, the boundary conditions need to accommodate equation (1). The acoustic/poroelastic and elastic/poroelastic coupling conditions will be presented next. Simpler boundary conditions (a rigid wall, imposed pressure, imposed displacements) can be directly derived from the two formulations described below.

2.2.1. Poroelastic/acoustic coupling. In the case of a poroelastic medium linked to an acoustic medium, system (7) states the continuity of the total normal stress, acoustic pressure and fluid flow.

$$\begin{aligned} \underline{\underline{\sigma}}^{\mathrm{t}} \cdot \underline{n} &= -p^{\mathrm{a}} \underline{n}, \\ p &= p^{\mathrm{a}}, \\ (1-\phi)\underline{u^{\mathrm{s}}} \cdot \underline{n} + \phi \underline{U^{\mathrm{f}}} \cdot \underline{n} &= \frac{1}{\rho_0 \omega^2} \underline{\nabla} p^{\mathrm{a}} \cdot \underline{n}, \end{aligned} \tag{7}$$

where p^{a} is the pressure in the acoustic medium, ρ_0 its density and $\underline{\underline{\sigma}}^{\mathrm{t}}$ the total stress tensor in the poroelastic material. Equations (8) and (9) express the well-formulated vectors $\underline{G}$ and $\underline{R}$.

$$\begin{bmatrix} G_i \\ G_4 \end{bmatrix} = \begin{bmatrix} \left\{ 1 - \phi \left(1 + \frac{\tilde{\lambda}^{\mathrm{sf}}}{\tilde{\lambda}^{\mathrm{f}}} \right) \right\} p^{\mathrm{a}} n_i \\ 0 \end{bmatrix}, \tag{8}$$

$$\begin{bmatrix} R_i \\ R_4 \end{bmatrix} = \begin{bmatrix} 0 \\ p - p^{\mathrm{a}} \end{bmatrix}. \tag{9}$$

Moreover, the continuity of fluid flow at the coupling interface can be expressed as an acceleration imposed upon the fluid in the acoustic medium. By substituting p for $\underline{U^{\mathrm{f}}}$ using equation (10), the correct normal acceleration can be obtained, as written in equation (11).

$$\underline{U^{\mathrm{f}}} = \frac{\phi}{\omega^2 \tilde{\rho}^{22}} \underline{\nabla} p - \frac{\tilde{\rho}^{12}}{\tilde{\rho}^{22}} \underline{u^{\mathrm{s}}}, \tag{10}$$

$$\begin{aligned} \frac{1}{\rho_0} \underline{\nabla} p^{\mathrm{a}} \cdot \underline{n} = \omega^2 \left[\underline{u^{\mathrm{s}}} \cdot \underline{n} \left(1 - \phi \left(1 + \frac{\tilde{\rho}^{12}}{\tilde{\rho}^{22}} \right) \right) \right] \\ + \omega^2 \left[\underline{\nabla} p \cdot \underline{n} \left(\frac{\phi^2}{\omega^2 \tilde{\rho}^{22}} \right) \right]. \end{aligned} \tag{11}$$

2.2.2. Poroelastic/elastic coupling. The poroelastic material is assumed to be bonded onto an elastic solid, which encompasses total continuity between the solid phase and elastic displacements. The total normal stress is also to be conserved. Moreover, one additional condition is needed to ensure the absence of relative fluid flow at the interface. System (12) summarizes these coupling formula.

$$\begin{aligned} \underline{\underline{\sigma}}^{\mathrm{t}} \cdot \underline{n} &= \underline{\underline{\sigma}}^{\mathrm{e}} \cdot \underline{n}, \\ \underline{u^{\mathrm{s}}} &= \underline{u^{\mathrm{e}}}, \\ \underline{U^{\mathrm{f}}} \cdot \underline{n} - \underline{u^{\mathrm{s}}} \cdot \underline{n} &= 0 \end{aligned} \tag{12}$$

where the superscript '.$^{\mathrm{e}}$' indicates the data relative to the elastic solid. The continuity of elastic and solid phase displacements can be easily achieved. Once reformulated, other conditions lead to equations (13) and (14).

$$\begin{bmatrix} G_i \\ G_4 \end{bmatrix} = \begin{bmatrix} -\phi \left(1 + \frac{\tilde{\lambda}^{\mathrm{sf}}}{\tilde{\lambda}^{\mathrm{f}}} \right) p n_{\mathrm{i}} - \sigma^{\mathrm{e}}_{ij} n_j \\ -\frac{\omega^2}{\phi} (\tilde{\rho}^{12} + \tilde{\rho}^{22}) u^{\mathrm{s}}_i n_i \end{bmatrix}, \tag{13}$$

Table 1. Poroelastic parameter of the studied felt.

h (m)	ϕ	σ (N s m^{-4})
2×10^{-2}	0.98	33 000
α_∞	Δ (m)	Δ' (m)
1.1	50×10^{-6}	110×10^{-6}
ρ_{pr} (kg m^{-3})	E_{pr} (Pa)	υ_{pr}
60	100 000 (1 + 0.88j)	0

$$\begin{bmatrix} R_i \\ R_4 \end{bmatrix} = \begin{bmatrix} u^{\mathrm{e}}_i - u^{\mathrm{s}}_i \\ 0 \end{bmatrix}. \tag{14}$$

It should be noted that the cases of an imposed pressure or displacement field can be directly derived from equations (8) and (9), by simply keeping R_4 and G_i, and from equations (13) and (14) by considering just R_i and G_4. Lastly, system (1) is fully defined, and a variational property is obtained by the software. After the meshing step, the mass and stiffness matrices are assembled and the problem is solved.

2.3. Validation of the implemented poroelasticity model

Model accuracy is validated by studying the case of a one-dimensional porous sample bonded onto a rigid wall and impinged by a normal harmonic unit pressure field. This configuration is relevant since an analytical solution can be derived. No shear wave exists and the propagating wave can be considered as the sum of two compression waves. The parameters of the felt sample have been summarized in table 1. The configuration is modelled using a three-dimensional geometry with appropriate boundary conditions on lateral faces.

In the table, j is the imaginary unit, $\mathrm{j}^2 = -1$. ϕ once again stands for the porosity. σ, α_∞, Δ and Δ' are the flow resistivity, tortuosity, and characteristic viscous and thermal lengths, respectively. These parameters are sufficient for applying the equivalent-fluid model of Johnson and Allard [6]. E_{pr}, ρ_{pr} and υ_{pr} are the Young's modulus, density and Poisson's ratio of the poroelastic material, respectively. With these coefficients, the Biot–Johnson–Allard theory is fully applicable. The finite-element calculation has been carried out for various meshes and two shape functions called *shlag2* and *shlag3* for the quadratic and cubic Lagrange polynomials. For better comprehension, the mesh denomination of the sample square cross-section is explained in figure 1. The 2D mesh partition will be that used for studying the whole hybrid panel. The final 3D mesh used for solving the problem is obtained by extruding this 2D mesh. As an example, a {7|8|4} 3D mesh denotes $M = 7$, $N = 8$ and four extruded layers from 0 to h.

Figure 2 shows the real and imaginary parts of the surface impedance Z_{s} at normal incidence, which is defined as the complex ratio of the acoustic pressure and total velocity at the impinged face. Since the amplitude of the incident pressure front is 1 Pa and considering the propagation axis to be x_3, Z_{s} can be stated as in equation (15).

$$\begin{aligned} Z_{\mathrm{s}}(\omega) &= \left[\mathrm{j}\omega \left(\phi U^{\mathrm{f}}_3 + (1-\phi) u^{\mathrm{s}}_3 \right) \right]^{-1}, \\ &= \left[\mathrm{j}\omega \left\{ \frac{\phi^2}{\omega^2 \tilde{\rho}^{22}} p_{,3} + \left(1 - \phi \left(1 + \frac{\tilde{\rho}^{12}}{\tilde{\rho}^{22}} \right) \right) u^{\mathrm{s}}_3 \right\} \right]^{-1}. \end{aligned} \tag{15}$$

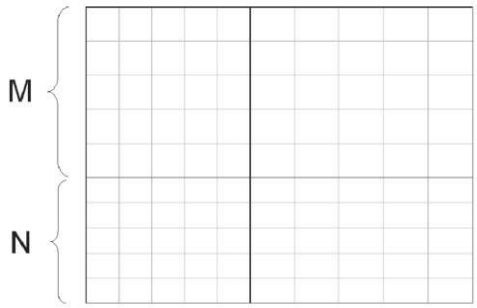

Figure 1. 2D mesh of the cross-section of the porous sample. Two parameters (M and N) are needed to generate a quad mesh. These meshes are denominated $\{M|N\}$.

The real and imaginary parts of Z_s exhibit good agreement between the exact and approximated solutions. The relative error does not exceed the 2% value attained for the *shlag2* {7|8|4} 3D mesh case. These discrepancies are present for both the real and imaginary parts but are not visible on the imaginary plot due to the range used. It is important to point out that the *shlag3* {5|5|2} 3D mesh and the *shlag2* {7|8|4} 3D mesh cases, which have the same number of nodes, lead to different results. Moreover the *shlag2* {7|8|6} case displays more nodes than the *shlag3* case and still approximates the same results. This behaviour is due to differences in the way the pressure gradient is calculated. The use of a second-order polynomial shape function for p involves a linear interpolation for the pressure gradient and then a biased approximation of fluid displacement. Figure 3 shows the approximated pressure gradient for various discrete cases; it reveals that a highly accurate finite-element formulation of the problem requires a polynomial of at least order 3. This conclusion tends to agree with previous results on the convergence of finite-element poroelasticity problems [8, 9]. To avoid prohibitive calculation time, the discretized formulation chosen for the entire panel study uses a second-order polynomial on a {5|5|4} mesh.

3. The coupled piezoelectric/elastic problem

The test case is a two-layer model made of a piezoelectric plate glued to a simply supported elastic plate, *i.e., the x_3 displacement is constrained at zero*. The lateral dimensions of the piezoelectric patch and the elastic material are different, which makes the coupling interface smaller than the entire meshed model. Two geometric configurations, involving different lateral dimensions and mass ratios, are studied. The forced harmonic responses of these systems to an applied electric potential on the upper face of the patch will be examined and the results obtained from *Comsol* compared to reference data from *Ansys*. Figure 4 depicts the typical study configuration. Symmetry considerations allow for modelling just a quarter of the sandwich. It should be noted that in both software applications, complete three-dimensional modes are considered, while the use of shell elements would decrease the calculation time. This choice has been motivated by the fact

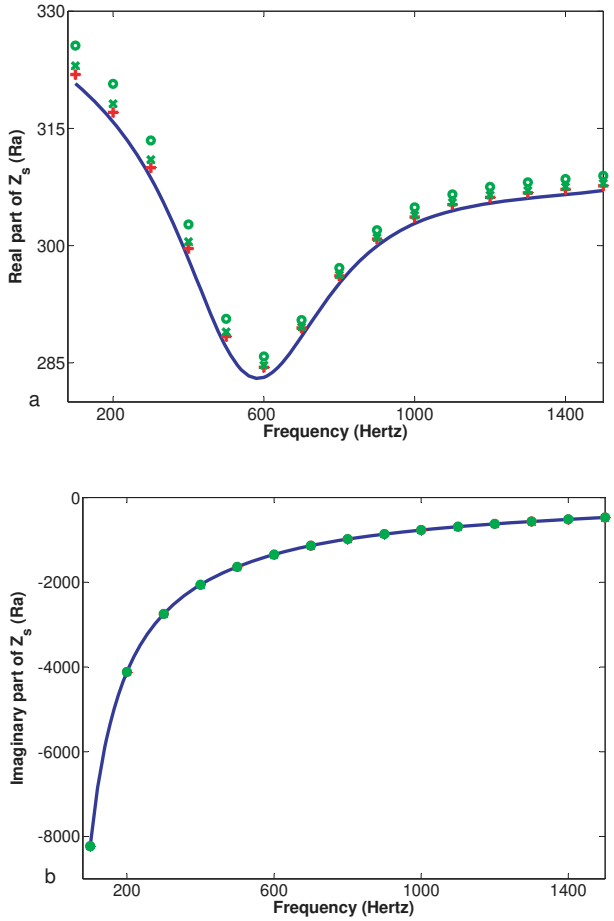

Figure 2. Real (a) and imaginary (b) parts of the surface impedance for the felt sample. (—) Analytical solution, (++) *shlag3* {5|5|2} 3D mesh, (○○) *shlag2* {7|8|4} 3D mesh and (××) *shlag2* {7|8|6} 3D mesh.

that *Comsol* provides no quad-mapped mesh for the Mindlin plate application mode. The elastic–solid and piezoelectric *Comsol* application modes are then used.

3.1. Similarly shaped layers

The first configuration contains a 55×55 mm^2 elastic plate, of thickness 0.3 mm. Its density, Young's modulus and Poisson's ratio are 2700 kg m^{-3}, 6.85×10^{10} Pa and 0.3, respectively. The square piezoelectric (*piezo 1*) patch has 38 mm edges and is 0.19 mm thick. Table 2 lists its elasticity parameters and dielectric properties. All materials are presumed to be isotropic. The two layers are discretized using second-order interpolation (*shlag2*). Meshes are denominated by merely their lateral number of elements $\{M|N\}$ since the thickness of both the plate and piezoelectric patch are discretized using just one element.

Figure 5 shows the x_3 displacement of the lower symmetric edge of the elastic plate (the bold line on figure 4). The two chosen frequencies, 100 and 1500 Hz, correspond to the extrema of the frequency range targeted in this study. The *Comsol* results agree very well with *Ansys* reference results. The relative error for converged meshes lies at 3% between the two software applications at a frequency of

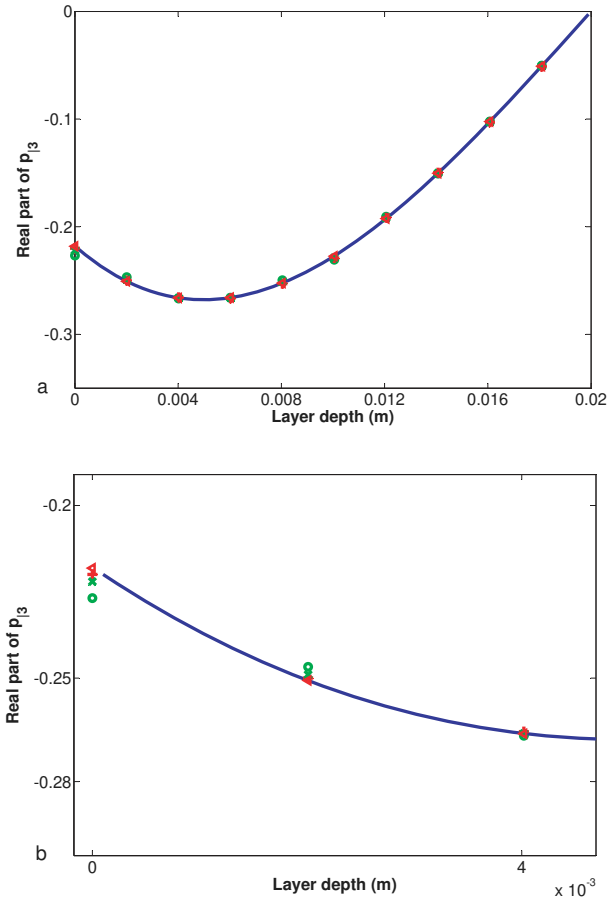

Figure 3. Real part of the pressure gradient at frequency 200 Hz. (a) Total depth. (b) Close-up view near the impinged depth. (—) Analytical solution, (◁) *shlag3* {5|5|4} 3D mesh, (++) *shlag3* {5|5|2} 3D mesh, (○○) *shlag2* {7|8|4} 3D mesh and (××) *shlag2* {7|8|6} 3D mesh.

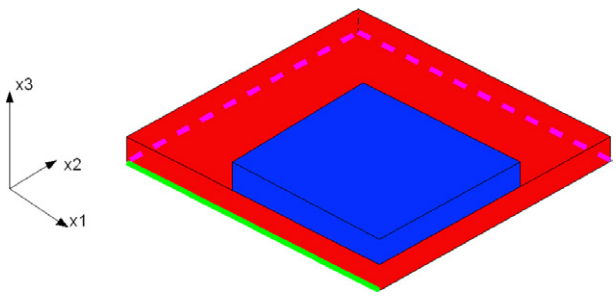

Figure 4. Model of a quarter piezoelectric/elastic configuration. The electric potential is applied to the upper face of the patch. Dashed line: simply supported edges, bold line: picked up data.

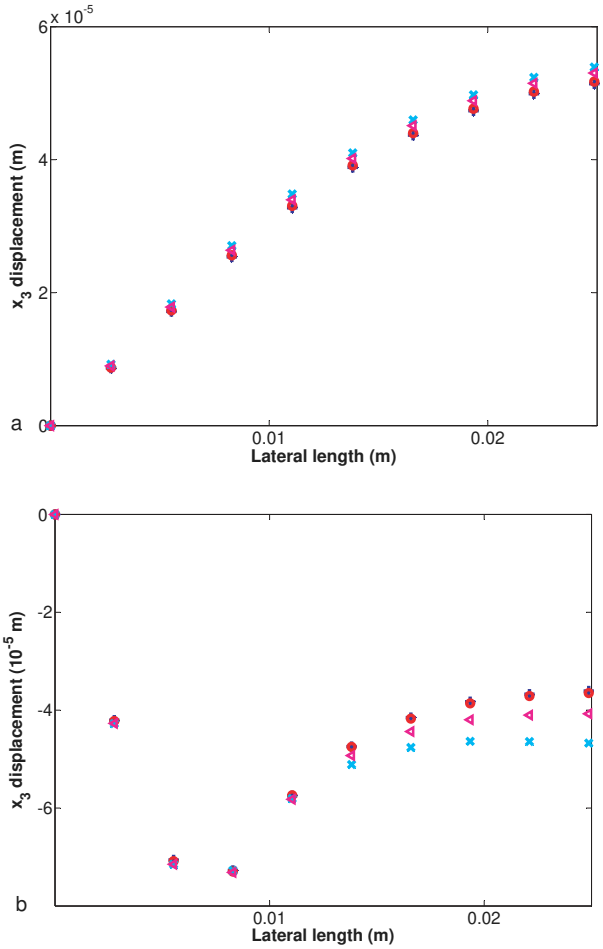

Figure 5. x_3 displacement on the lowest symmetric edge for piezoelectric/elastic configuration 1. (a) Frequency 100 Hz, (b) frequency 1500 Hz. (++) *Comsol shlag2* {5|5}, (××) *Ansys shlag2* {5|5}, (○○) *Comsol shlag2* {10|10}, (◁) *Ansys shlag2* {10|10}.

Table 2. Piezoelectric (*piezo 1*) properties.

E_{pi1} (Pa)	υ_{pi1}	ρ_{pi1} (kg m^{-3})	
9.6×10^{10}	0.34	7650	
e_{31} (C m^{-2})	e_{33} (C m^{-2})	ε_{11}	ε_{33}
−6.18	6.18	1142	668

100 Hz. It must be stressed that the two *Comsol* calculations with different discretizations yield very similar results. The same study, conducted at a frequency of 1500 Hz, reveals larger discrepancies of 5%. It seems that the *Ansys* model is not converged for this discretization. The more complicated behaviour of the sandwich at this frequency explains the slower mesh convergence. Once again however, the two *Comsol* results are similar. This finding stems from the fact that *Ansys* provides incomplete Lagrange quad elements, whereas *Comsol* provides complete Lagrange elements. The resulting degrees of freedom for the two software applications are then dissimilar for an equivalent mesh. The fact that the *Ansys*{10|10} results differ less from *Comsol*'s calculated displacement than {5|5} from the mesh supports this explanation. Furthermore, the coupling between elastic and piezoelectric materials, using pre-established *Comsol* application modes, is validated.

3.2. Differently shaped layers

The second configuration entails a 66×66 mm^2 elastic plate, of thickness 0.2 mm. Its density, Young's modulus and Poisson's ratio are 7700 kg m^{-3}, 2×10^{11} Pa and 0.27, respectively. The piezoelectric patch is different from the previous case. This

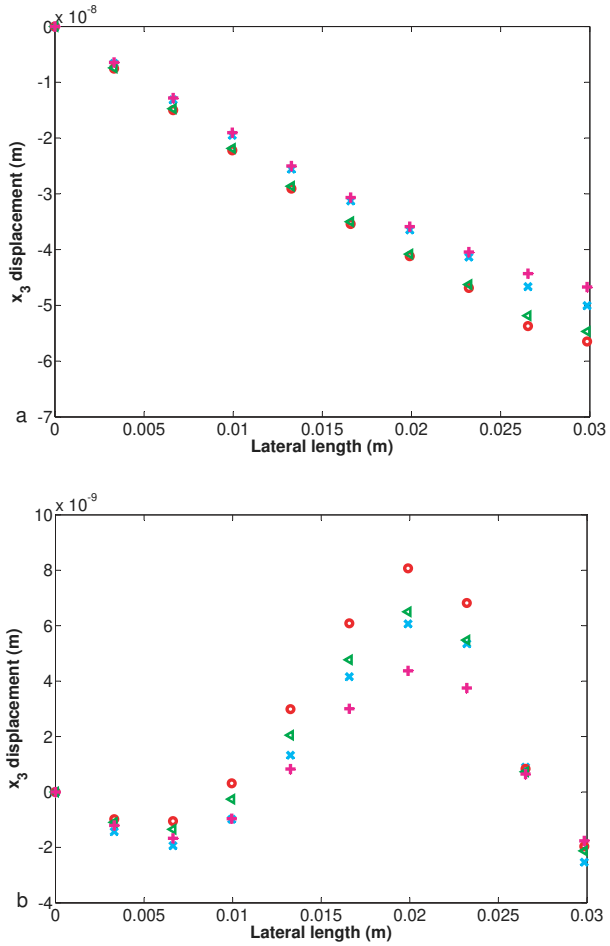

Figure 6. x_3 displacement on the lowest symmetric edge for piezoelectric/elastic configuration 2. (a) Frequency 100 Hz, (b) frequency 1500 Hz. ($\times\times$) *Comsol shlag2* {8|8}, (OO) *Comsol shlag2* {10|10}, ($\triangleleft$) *Comsol shlag3* {8|8}, (++) *Comsol shlag3* {10|10}.

Table 3. Piezoelectric (*piezo 2*) properties.

E_{pi2} (Pa)	υ_{pi2}	ρ_{pi2} (kg m^{-3})	
7×10^{11}	0.3	14 435	
d_{31} (C m^{-2})	d_{33} (C m^{-2})	ε_{11}	ε_{33}
-186×10^{-12}	0	1850	1850

material, called *piezo 2*, contains a cross section of 15×15 mm^2 and is 2 mm thick. Table 3 lists the associated physical properties, which are completely different from *piezo 1*. This time, displacements calculated only by using *Comsol* have been plotted in figure 6. The elastic plate is discretized with one element over its thickness, as opposed to the piezoelectric material, which has four thickness elements.

The mesh does not seem to converge for the same lateral {5|5} discretization as in the previous case. The use of cubic polynomial shape functions apparently does not increase the convergence rate. In fact, a {10|10} lateral discretization of the sandwich, with four elements in the thickness of the piezoelectric material, is still not sufficient

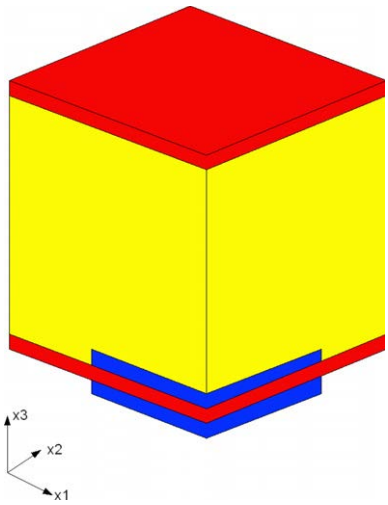

Figure 7. A quarter panel, configuration B–B with active patches bonded onto the incident plate. The impinging acoustic wavefront is normal to x_3.

Table 4. Poroelastic parameters of the rock wool.

h (m)	ϕ	σ (N s m^{-4})
2×10^{-2}	0.94	40 000
α_∞	Δ (m)	Δ' (m)
1.1	56×10^{-6}	110×10^{-6}
ρ_{pr} (kg m^{-3})	E_{pr} (Pa)	υ_{pr}
130	4400 000 (1 + 0.1j)	0

at frequency 1500 Hz. Differences in the dynamic behaviour between distinct layers seems to exert considerable influence on the required level of mesh refinement. Discretization has not been further investigated since the calculation time was already approximately 3 min per frequency using a Pentium 4 processor with sufficient memory to use the fastest solver. This case illustrates that classic meshing rules are not applicable to a coupled problem. Each configuration has to be tested and meshed separately. Furthermore, the use of shell elements would allow using finer elements for the piezoelectric material without wasting nodes, and hence calculation time, for the elastic plate thickness. This assessment would have to be tested when the quad mesh for the Mindlin plate application mode is implemented in *Comsol*.

4. Modelling the entire hybrid panel

The entire panel (see figure 7) is modelled, thanks to the *Comsol* environment, by taking into account the previous remarks. The lateral dimensions are 66×66 mm^2. The 2 cm core is made of either felt (see table 1 above) or rock wool, whose characteristics are summarized in table 4. This core is sandwiched by two elastic plates 0.2 mm thick with properties given in section 3.2. The piezoelectric patches are those described in table 2, with a squared section of 38×38 mm^2 and a thickness of 0.19 mm. For all layers, the surface mesh is the {5|5} version, and shape functions are

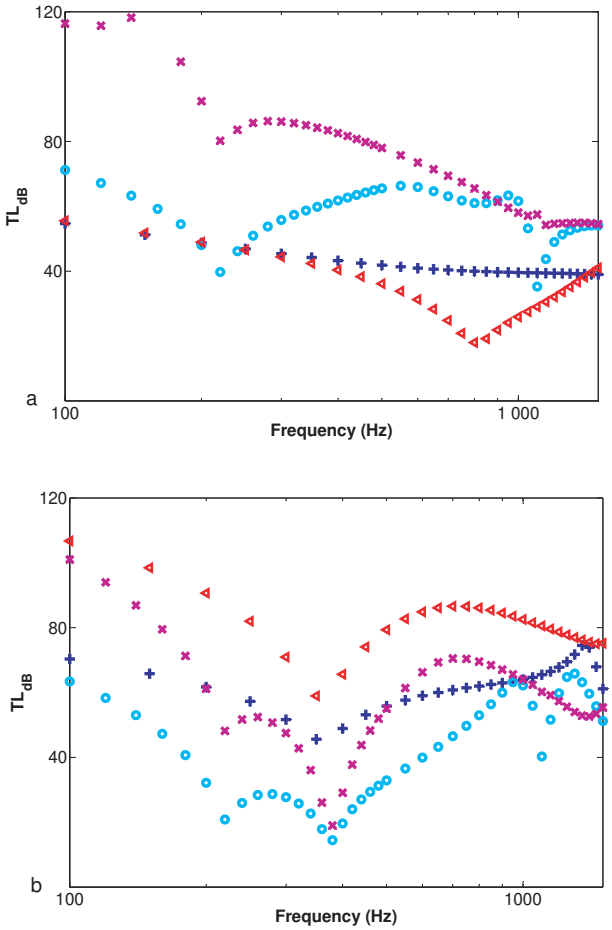

Figure 8. Passive and active transmission losses with piezoelectric patches glued onto the impinged plate. (a) Rock wool core. (b) Felt core. (○○) Passive B–G configuration, (××) active B–G configuration, (++) passive B–B configuration, (◁) active B–B configuration.

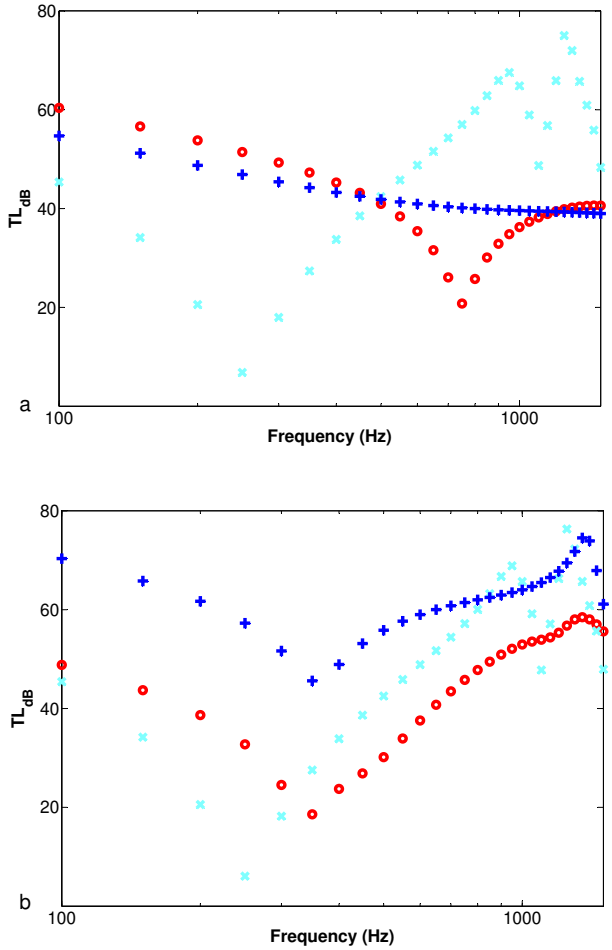

Figure 9. Passive transmission losses for the B–B configuration with piezoelectric patches glued to the impinged plate and different cores. (a) Rock wool core. (b) Felt core. (++) Poroelastic core, (××) porous core with rigid frame, (○○) elastic solid core with poroelastic skeleton properties.

a second-order Lagrange polynomial. The piezoelectric and elastic layers have one thickness element, and the poroelastic core is discretized using four thickness elements. The piezoelectric/elastic and poroelastic/elastic coupling are fully considered. This configuration was shown above to yield sufficiently, although not totally, converged results to carry out a qualitative parametric study with a 'relatively' acceptable calculation time. The case of rock wool was not treated in section 2.3 since convergence results are similar to those obtained for the felt.

The sandwich boundary conditions are ideal. The two elastic faceplates are simply supported, and the normal displacement of lateral faces of the core is blocked. The actuating solution chosen involves two pieces of piezoelectric material glued to the impinged elastic plate. This two patches are polarized to deform in phase opposition. This bimorph solution has not been tested on the radiating plate due to its lack of practical applicability caused by the control strategy developed. The error sensor must indeed be bonded to the radiated plate in order to monitor normal displacement. Two passive stacks containing the core, to be fully coupled (*B–B configuration*) to both elastic plates or a 2×10^{-6} m air gap between the core and the radiating plate (*B–G configuration*), are modelled.

Lastly, for all these configurations, the panel is impinged by a harmonic unit amplitude pressure field under normal incident, and both passive and active responses are calculated. The following sections will detail the significant qualitative results. The transmission loss ($\mathrm{TL_{dB}}$) [10] defined in equation (16) is used as a performance indicator, along with the direct results.

$$\mathrm{TL_{dB}} = 10 \log_{10} \frac{W_\mathrm{i}}{W_\mathrm{t}}, \tag{16}$$

where W_i and W_t are the incident and transmitted energies, respectively.

4.1. Passive panel properties

The passive and active transmission losses for the two core materials have been plotted in figure 8, for frequencies between 100 and 1500 Hz. The passive performance of the felt panel is better with the B–B configuration than with the B–G set-up. This behaviour is totally opposite that observed for

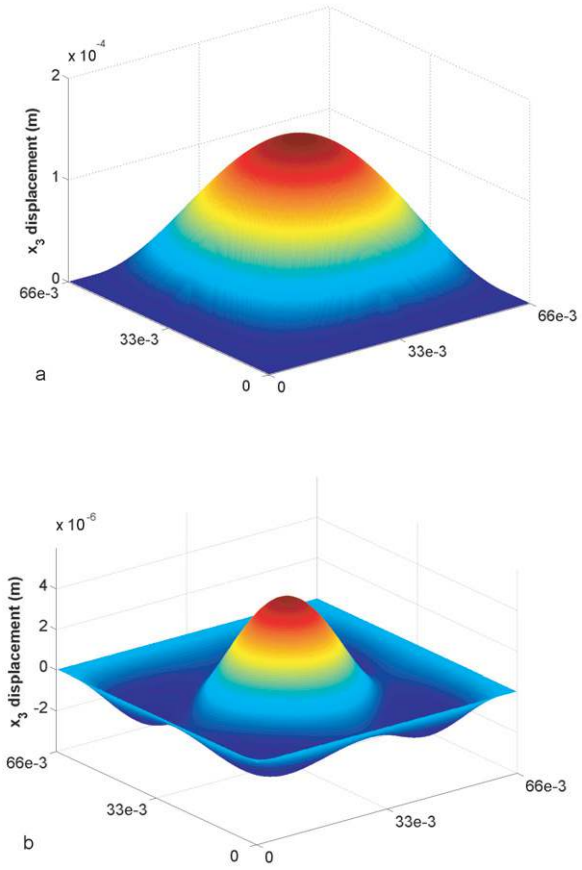

Figure 10. Deformation of the radiating plate for the piezoelectric patches glued to the impinged plate. (a) Frequency 220 Hz. (b) Frequency 1100 Hz.

the rock wool panel. Figure 9 shows passive transmission losses for the same layer configuration yet with three different core models that include the previously described poroelastic model, the equivalent-fluid model and the 'equivalent-solid' model. The latter model describes the mid-layer as an elastic solid with elastic properties similar to those of the poroelastic skeleton. The calculated attenuations illustrate the solid phase dependence of the poroelastic dynamic response.

The *B–G* configuration highlights two frequencies where the panel is acoustically transparent. Transmission loss is in fact driven by the response of the radiating plate. At a frequency of 220 Hz, coincidence with the 1–1 plate mode starts to appear. At a frequency of 1100 Hz, the losses decrease once again, due to coincidence with both the 3–1 and the 1–3 resonant frequencies of the square plate. The deformed shape is then a combination of these two modes, as plotted in figure 10. These remarks are also applicable to the configuration where a single piezoelectric patch is glued to the radiating plate. The transmitted wave is then controlled by the piezoelectric/elastic dynamic behaviour. These singularities do not depend on the poroelastic material for these ideal lateral boundary conditions applied to the core and therefore constitute specific issues that may be easily designed by choosing appropriate elastic plate properties.

4.2. Active panel properties

The applied active control strategy used in figure 8 is aimed at minimizing the out-of-plane displacement at the centre of the radiating plate. First, the panel is excited by an incident pressure wave and the P_0 transfer function is calculated. Second, a unit voltage is applied to piezoelectric patches and the V_0 transfer function is then obtained. Next, the linearity of the physics involved allows applying the superposition principle to calculate the suitable voltage for achieving the control.

Results indicate a significant increase in transmission loss for the *B–G* felt panel. Previously described resonant modes of the *B–G* configuration are well reduced, and only the *double-leaf* resonance at 400 Hz remains. Improved performance is obtained for the *B–G* rock wool panel, whereas the *B–B* case illustrates an active strategy yielding unwanted results. The transmission loss decreases over the entire frequency range studied. The primary source excites the impinged plate with a deformed shape with a similar appearance as a 4-antinode mode. Once the wave has propagated through the core, the output plate radiates mainly on its 1–1 mode. The secondary path then does not preserve shape. Similarly, the piezoelectric patches deforming the impinged plate will deform the radiating plate near the same 4-antinode mode with very little displacement at the centre. During active control, interferences between the primary pressure source and the vibrational secondary source are constructive, as shown in figure 11. This dysfunction can be partially overcome by minimizing the out-of-plane displacement of the radiating plate over a finite area, but not by gluing a single piezoelectric material onto the upper plate instead of the incident plate, as shown in figure 12. This latter solution was tested on other panel configurations but was not selected herein since active/passive results were generally not as good as those calculated from a panel with patches on the incident plate. Moreover, different piezoelectric matrices have been used that involve just e_{31}, e_{32} or e_{33} coupling terms. Active results were quite similar with equivalent voltages and are not reported in this paper.

This initial study exhibits the qualitative reliability of the whole panel model. As discussed previously, quantitative results could not be derived due to the need for refined meshes that dramatically increase the calculation time. Nevertheless, qualitative trends have been illustrated. The choice between a partially glued and a totally glued panel thus depends on the core elastic properties. An overly stiff core will be less efficient and hard to actively control if totally bonded onto the incident and radiating plates. In contrast, an airgap will optimize the transmission losses even if it is being controlled by resonant plate modes. Such resonances are well localized and then become reasonable targets for available control algorithms. For the panel studied, piezoelectric patches need to be placed on the impinged plate. Finally, the overall passive/active performance for piezoelectric patches glued onto the radiating plate is not as good as in the case with patches glued onto the incident plate.

5. Numerical and experimental comparison

This section presents a comparison between calculated and experimental TL_{dB} for a hybrid panel. The elastic plates are

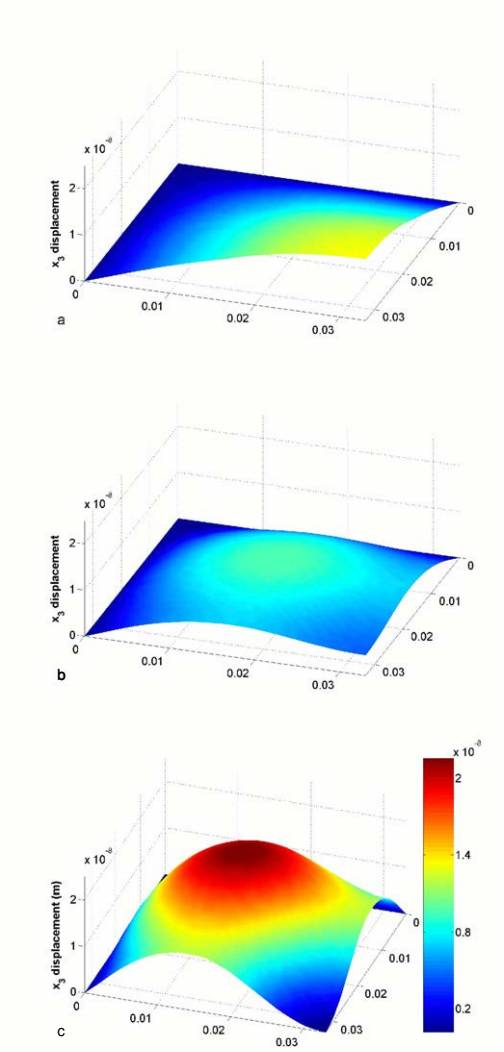

Figure 11. Out-of-plane absolute displacement of the quarter radiating plate for rock wool core in the B–B configuration with active patches onto the incident plate. (a) Unit pressure excitation. (b) Unit voltage excitation. (c) Unit pressure with active control.

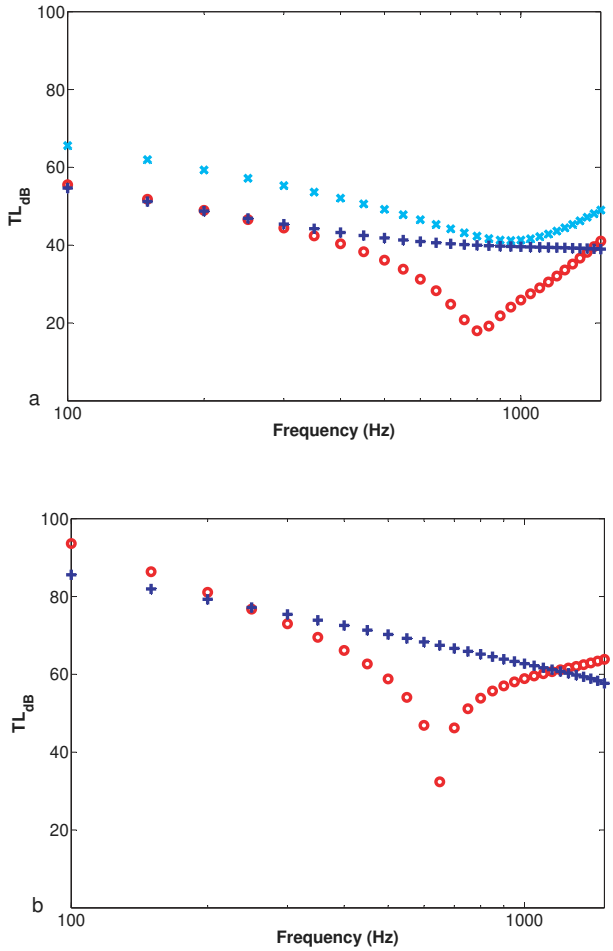

Figure 12. Active and passive TL_{dB} for rock wool core in the B–B configuration. (a) Piezoelectric patches glued to the incident plate. (b) Single piezoelectric patch glued to the radiating plate. (++) Passive results. (○○) Active minimization of the displacement at the radiating plate centre. (××) Active minimization of the radiating plate displacement over a finite area.

those used in the previous section. The piezoelectric patches are *piezo 2* and they are glued onto the impinged plate. The core is the 2 cm thick felt described in table 1. Experimental results have been obtained thanks to a specific set-up allowing us to measure transmission losses under normal incidence until reaching 2500 Hz. Figure 13 shows the passive and active TL_{dB} obtained experimentally and numerically for frequencies ranging from 0 to 500 Hz.

Both results highlight an active increase in transmission losses at resonant frequencies of the panel. Discrepancies between numerical and experimental values are due to the difficulty involved in generating perfect simply supported experimental boundary conditions. Moreover, the coupling between layers is modelled using the B–G configuration, which is not experimentally true. The mesh used was the same {5|5} as the one above, which has shown to lead to non-convergent results. In addition, the experimental increase is not attained at very low frequencies, due to a lack of power supplied to the actuators. The piezoelectric material used is not optimal and the appropriate voltage was calculated to be more than 200 V. The hybrid concept has however been qualitatively validated, as has the finite-element model developed.

6. Conclusion

In this paper, a new multiphysics finite-element model of a hybrid piezoelectric/poroelastic sandwich panel has been discussed in detail. Implementation was performed using the *Comsol* environment. The complete formulation of the poroelastic problem was presented and validated by comparing the results with analytical solutions. The reliability study of each panel layer was conducted and mesh convergence was shown to be highly correlated with the shape functions used and the various physics scales involved. Several calculations focusing on different layer configurations and properties were also carried out. The initial qualitative results demonstrate the potential for enhancing transmission losses by the use of active control procedures. Moreover, the configuration with an airgap between the core and radiating plate was found to be a straightforward case for designing panel resonances. In

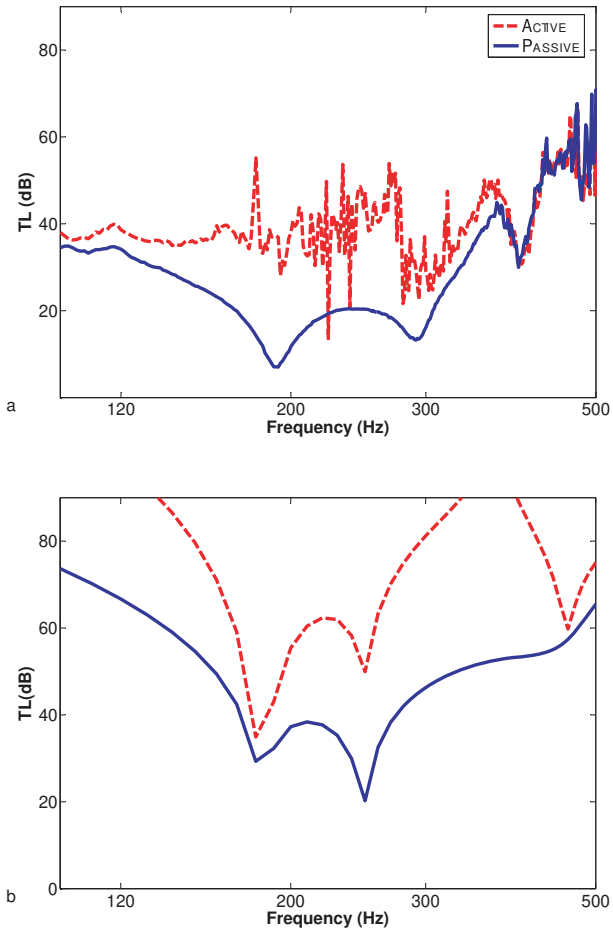

Figure 13. Comparison between experimental (a) and predicted (b) TL_{dB}. Solid line: passive mode, dashed line: active mode.

contrast, the bonded–bonded panel was found to depend upon poroelastic properties in a complex manner, and to offer limited active controllability. Lastly, the concept of an active/passive panel was proven to be experimentally conceivable. The next step consists of quantitatively optimizing such sandwiches. However, while the model developed was shown to be robust, the calculation time still prevents an optimization study from being performed. The use of sub-structuring techniques is now envisaged.

References

[1] Guigou C and Fuller C R 1999 Control of aircraft interior broadband noise with foam-pvdf smart skin *J. Sound Vib.* **220** 541–57

[2] Johnson B D and Fuller C R 2000 Broadband control of plate radiation using a piezoelectric, double-amplifier active-skin and structural acoustic sensing *J. Acoust. Soc. Am.* **107** 876–84

[3] Carneal J P and Fuller C R 2004 An analytical and experimental investigation of active structural acoustic control of noise transmission through double panel system *J. Sound Vib.* **272** 749–71

[4] Galland M-A, Mazeaud B and Sellen N 2005 Hybrid passive/active absorbers for flow ducts *Appl. Acoust.* **66** 691–708

[5] Zielinski T G, Galland M-A and Ichchou M N 2005 Active reduction of vibroacoustics transmission using elasto-poroelastic sandwich panels and piezoelectric materials *Proc. 1st Symp. on the Acoustic of Poroelastic Material*

[6] Allard J-F 1993 *Propagation of Sound in Porous Media: Modelling Sound Absorbing Materials* (New York: Elsevier Applied Science)

[7] Atalla N, Panneton R and Debergue P 1998 A mixed displacement-pressure formulation for poroelastic materials *J. Acoust. Soc. Am.* **104** 1444–52

[8] Rigobert S, Atalla N and Sgard F C 2003 Investigation of the convergence of the mixed displacement-pressure formulation for three-dimensional poroelastic materials using hierarchical elements *J. Acoust. Soc. Am.* **114** 2607–17

[9] Hörlin N E 2005 3d hierarchical hp-fem applied to elasto-acoustic modelling of layered porous media *J. Sound Vib.* **285** 341–63

[10] Lesueur C 1988 *Rayonnement Acoustique des Structures* (Paris: Eyrolles)